iScience

CellPress
OPEN ACCESS

Article

Probing atomic structure of beam-sensitive energy materials in their native states using cryogenic transmission electron microscopes

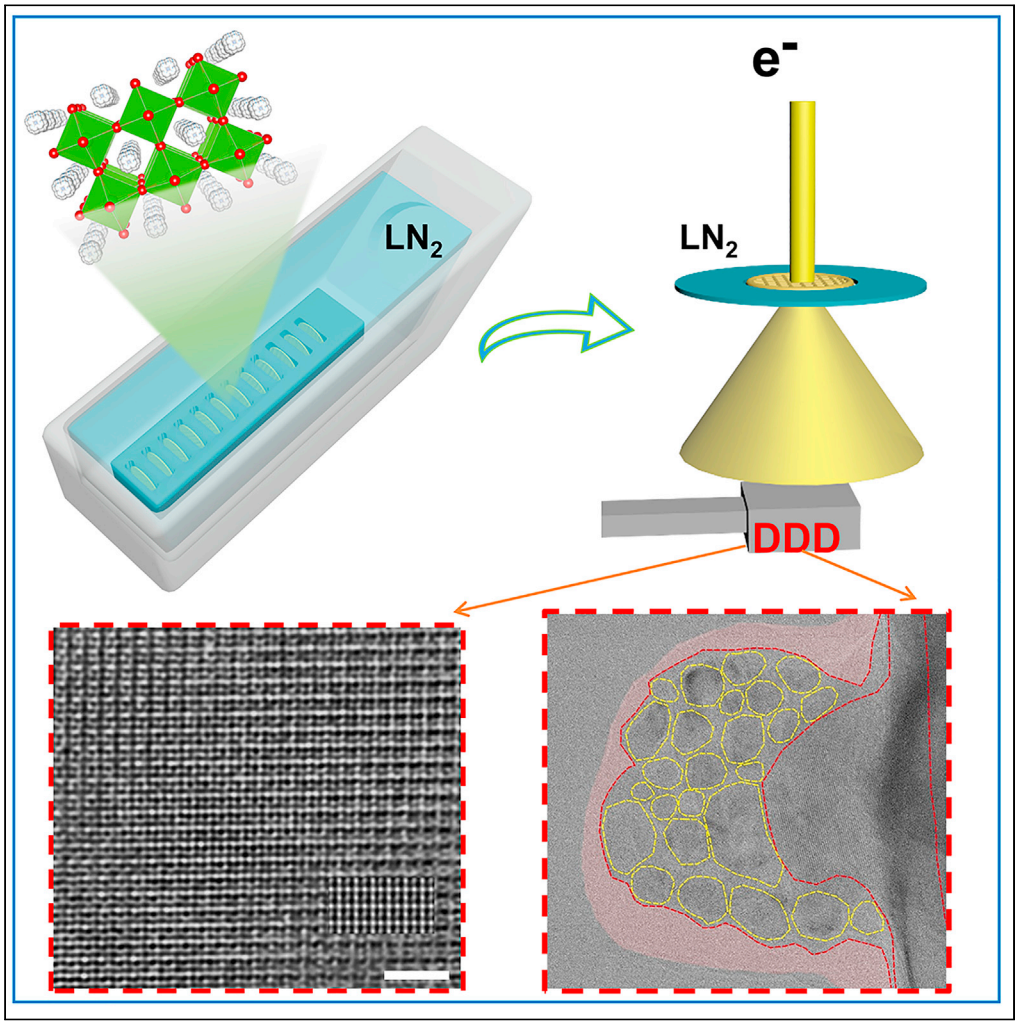

Yuanmin Zhu, Qing Zhang, Xuming Yang, Menghao Li, Biao Wang, Meng Gu

gum@sustech.edu.cn

Highlights

Hybrid beam-sensitive materials characterized at the atomic scale using cryo-TEM

Structural evolution from an initial metastable state to the perfect crystalline observed

Na nuclei and its organic SEI structures acquired at the first cycle of Na batteries

Zhu et al., iScience *24*, 103385
November 19, 2021
https://doi.org/10.1016/j.isci.2021.103385

iScience

CellPress
OPEN ACCESS

Article

Probing atomic structure of beam-sensitive energy materials in their native states using cryogenic transmission electron microscopes

Yuanmin Zhu,[1,2] Qing Zhang,[2] Xuming Yang,[2] Menghao Li,[2] Biao Wang,[1] and Meng Gu[2,3,*]

SUMMARY

Organic–inorganic hybrid perovskite nanoplatelets (NPLs) have emerged as promising materials for solar energy. However, the structural instability under electron beam hinders further probing and understanding of its crystalline structures and defects at the atomic scale. Taking methylammonium bromide perovskite methylammonium lead bromide ($CH_3NH_3PbBr_3$ ($MAPbBr_3$)) perovskite NPLs as model material, we performed atomic-scale characterization of the native state of the hybrid perovskite solar cell material in different states using ultra-low-dose cryo-TEM imaging. With a series of observation at different growth time, we revealed the growth pattern of such $MAPbBr_3$ material from an initially stacked slices with rotational moiré fringes to a perfect single-crystalline structure of NPLs. Our high-resolution cryo-TEM further enabled the atomic-scale investigations of solid electrolyte interphase (SEI) and sodium (Na) dendrite materials, which can largely impact the safety and life of batteries. This study offers insights on the atomic scale characterization of a wide variety of beam-sensitive materials, inspiring us to probe more materials with cryo-transmission electron microscopes (TEM).

INTRODUCTION

For materials science research, understanding the fundamental structure–property relationships of functional materials is key, and transmission electron microscopy (TEM), especially high-resolution TEM (HRTEM), has proven to be a powerful tool for the structural characterization of condensed materials (Arenholz et al., 2016; Hayat, 2012; Williams and Carter, 1996; Ye et al., 2021; Zhu et al., 2020b). However, a wide range of soft materials is easily damaged by the high-voltage electron beams, including organic–inorganic hybrid materials such as halide hybrid perovskites with appealing optoelectronic properties, alkali metal batteries with a solid-state electrolyte layer, and metal–organic frameworks (MOFs) with fascinating catalytic properties (Chen et al., 2015; Hong et al., 2018; Lei et al., 2020; Lin et al., 2014; Rothmann et al., 2020; Stock and Biswas, 2012). Thus, the primary challenge for TEM characterization has been to probe the atomic microstructures of these fragile organic–inorganic hybrid materials without causing severe beam damage or introducing artifacts into the sample.

The exact causes and mechanisms of beam damage are complicated and vary depending on the properties of the material sample, but they can be loosely identified as knock-on damage, radiation damage, and heating effects (Egerton, 2012; Ghosh et al., 2019). Consequently, some effective routes have been proposed to alleviate beam damage on the beam-sensitive materials, that is, reducing the energy of electron beam, decreasing the dosage of the beam, and characterizing in a low-temperature environment. These methods have achieved obvious progress (Hashimoto et al., 2004; Sawada et al., 2015), but low accelerating voltages and low electron dosage usually result in poor image resolution, low signal-to-noise ratio, and a strict restriction of sample thickness. Similarly, the use of cryogenic sample holders in conventional TEM has somewhat decreased heating damage; however, conventional charge-coupled device cameras (CCD) cannot produce HRTEM images with a sufficient signal-to-noise ratio for observations made at the extremely low electron dose rates which are required for beam-sensitive materials. Recently, cryogenic TEM (cryo-TEM) equipped with electron direct detection device cameras (DDD cameras) which enables highly efficient electron detecting has become widely used in structural biology to resolve protein structures under a low electron dose state (Bai et al., 2015).

[1]School of Materials Science and Engineering, Dongguan University of Technology, Dongguan 523808, China

[2]Department of Materials Science and Engineering, Southern University of Science and Technology, Shenzhen 518055, China

[3]Lead contact

*Correspondence: gum@sustech.edu.cn

https://doi.org/10.1016/j.isci.2021.103385

In particular, we consider that this technique will be useful for characterizing electron beam-sensitive materials in the field of materials science. First, single crystalline halide hybrid perovskites are the famous organic–inorganic hybrid energy materials, which are important for solar energy applications because their low electron-hole recombination means free paths enhance their carrier transport and stability. However, because any defects can modify the hybrid perovskite's transport of charge carriers, direct visualization of point defects, dislocations, or grain boundaries in the hybrid perovskites is urgently needed to deduce clear structure–property relationships. Organic–inorganic hybrid perovskites are easily degraded when exposed to light, air, moisture environments, and severely damaged by the high-voltage electron beams (Chen et al., 2018; Deng, 2021; Ran et al., 2020; Rothmann et al., 2018). For example, Nellist et al. recently used low-dose low-angle annular dark field scanning transmission electron microscopy to reveal clear grain boundaries, coherent perovskite–PbI_2 interfaces, and dislocations in the $FAPbI_3$ perovskite (Rothmann et al., 2020). Likewise, using cryo-TEM equipped DDD camera, our group recently discovered an important stacking-fault defect in single crystalline $MAPbI_3$, which showed improved thermodynamic structure stability and greatly modified the bandgap and recombination behavior of electrons and holes (Zhu et al., 2020a). Except for the single-crystalline or polycrystalline bulk phases, 2-dimensional (2D) perovskite NPLs have been intensively reported with thrilling quantum and dielectric confinement (Weidman et al., 2017; Yang et al., 2017); however, owing to its fast formation process and instability during growth, the underlying growth mechanisms and atomic structural evolution of the 2D hybrid nanoplate materials need further investigation.

Second, the solid electrolyte interphase (SEI) layer structure in alkali metal batteries, often containing organic components, is another type of organic–inorganic hybrid energy material. Direct atomic imaging of the SEI's phase components and their spatial arrangement is also challenging. Using ultralow-dosage cryo-TEM, our group has achieved to probe the SEI gradient amorphous and crystalline phase components of a lithium-metal anode (Han et al., 2021), and more detailed structural information of the SEI microstructures in alkali metal batteries needs to be explored urgently.

Here, taking methylammonium lead bromide nanoplatelets ($MAPbBr_3$ NPLs) as model materials, we report an atomic-scale characterization of organic–inorganic hybrid materials by low-dose cryo-TEM and a detailed investigation of the defect structure evolutions that reveals their fundamental growth mechanism. To further validate the broad applications of this cryo-TEM technology (illustrated in Figure S1), we also carried out an atomic-scale investigation of the native state of the initial alkali metals-SEI structures in the Na metal battery implied the participation of the organic electrolyte decomposition in the early stage of the SEI formation.

RESULTS AND DISCUSSION

Low electron dose cryo-transmission electron microscopes method

There are several improvements of our cryo-TEM method based on the current cryo-EM technology (Li et al., 2018; Wang et al., 2018; Zhu et al., 2020a). We applied cryo-TEM method steps as outlined in Figure S1. First, samples were dropped on a TEM-grid inside the Ar-filled glove box, and the specimen was immediately immersed into a liquid nitrogen box in the glove box. Thus, the specimen was protected and sealed by the liquid nitrogen until it was inserted into the cryogenic chamber of the cryo-TEM through the cryo-transfer auto-loader. This sample preparation procedure ensures that the sensitive materials were completely isolated from any trace of oxygen or moisture from the environment. Second, the cryo-TEM is an aberration-corrected cryo-TEM, which has a higher resolution limit than others. The spherical aberration of the TEM can be reduced to about −0.006 mm (C3), giving a strong ability of HRTEM imaging. Third, when acquiring images, the low dose mode in cryo-TEM is used, which is specially applied in life science. For different sensitive materials, the electron dose from ~1 to 20 e $Å^{-2}$ s^{-1} can be tuned in the low dose mode. At last, drift-correction, image post-processing, and simulation techniques are used to get better HRTEM data. For more details, it can be found in the methods part.

Probing the atomic structure of the hybrid halide methylammonium lead bromide nanoplatelets

The methylammonium bromide perovskite methylammonium lead bromide ($CH_3NH_3PbBr_3$ ($MAPbBr_3$)) phase has a cubic structure (*Pm-3m*) with a lattice of a = 5.9195 Å (Table S1), in which the MA organic groups occupy the A-site of the typical ABO_3 perovskite structure. The energy dispersive spectrum (EDS) of $MAPbBr_3$ NPLs shown in Figure S6 demonstrated the homogeneous distribution of C, N, Pb, Br elements in the NPLs and the result also illustrates the degradation of the NPLs in EDS acquiring process with a high

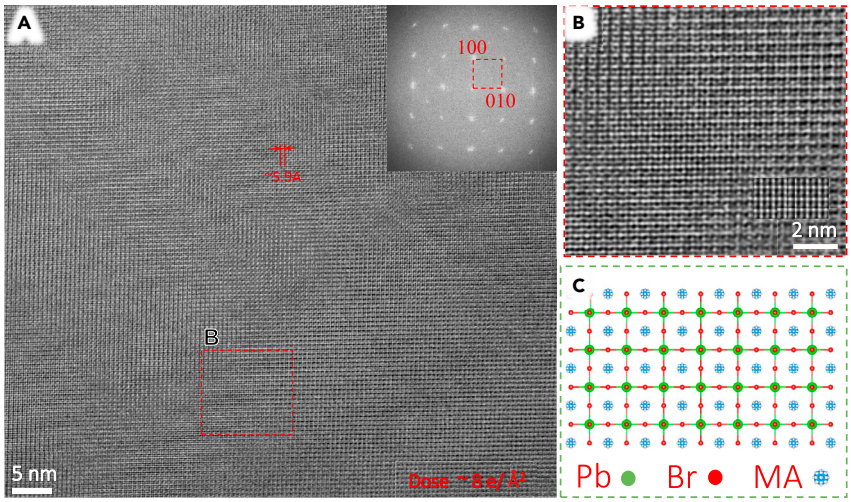

Figure 1. Cryo-HRTEM image of the atomic structure of the hybrid halide $MAPbBr_3$ NPL

(A) Atomic-resolution Cryo-HRTEM images of $MAPbBr_3$ NPL along the [001] direction with an accumulated electron dose of ~8 e $Å^{-2}$ (4 e $Å^{-2}$ s^{-1} for 2 s). The corresponding FFT pattern is shown as inset in the corner.

(B) Enlarged image of a selected area (red dashed box) from (A), depicting the atomic structure imaging of $MAPbBr_3$. The simulated HRTEM image of [001] $MAPbBr_3$ overlapped in the middle is well-consistent with the experimental HRTEM image.

(C) A structural model of the $MAPbBr_3$ along the [001] direction.

electron dose in the conventional TEM. By selecting a critical electron dosage (<10 e $Å^{-2}$ s^{-1}) in the cryo-TEM equipped DDD cameras, we could reliably image the native structure of $MAPbBr_3$ with atomic resolution. Figure 1 depicts an atomic resolution cryo-TEM image of the ideal single-crystalline $MAPbBr_3$ NPLs along the [001] axis at extremely low-dose (~4 e $Å^{-2}$ s^{-1}) conditions. In the cryo-HRTEM image (Figure 1A), {100} lattices with an average spacing of ~5.9 Å could be clearly observed and the fast Fourier transform (FFT) pattern provided in the inset illustrates the cubic perovskite structure. Figure 1B shows an enlarged image of the red dashed box in Figure 1A and offers further insights into the atomic structure of the $MAPbBr_3$. To confirm the atomic column positions, series of image simulations for the HRTEM image were performed using the standard $MAPbBr_3$ structure model. The simulated HRTEM image was calculated by the Mactempas software from the [001] $MAPbBr_3$ structure model shown in Figure 1C. After careful comparison, its atomic contrast in Figure 1B agrees well with that of the simulated HRTEM image (inset) of the $MAPbBr_3$ structure (detailed simulation results are provided in Figure S2). We clearly resolved the atomic positions for the PbBr columns (brightest contrast), Br columns (darker contrast, around the PbBr columns), and MA cations (darkest contrast, between the Br columns). Thus, we can confirm the atomic arrangement of the [001] $MAPbBr_3$ structural image, and distinguish the MA, PbBr, and Br positions for further analysis, respectively. One should note that the HRTEM images in Figure 1B show slight contrast change in some areas which may originate from the sample thickness variations.

The cryogenic temperature is ~77 K, and phase transition of the samples in this work may take place. In the FFT patterns of $MAPbBr_3$ NPLs shown as the inset of Figure 1A, we found that there are some additional weak reflections. According to the comparation with simulated electron diffraction patterns in Figure S3, the additional weak reflections belong to the orthorhombic phase (space group: $Pna2_1$, (Table S2)) of $MAPbBr_3$ which is a distorted perovskite from its cubic phase. Owing to the additional reflections are very weak, it is suggested that the phase transition only partially occurs in local areas. Furthermore, the HRTEM images of $MAPbBr_3$ with cubic structure usually were observed in our cryo-TEM experiments (Figure S8). Considering the samples were rapidly quenched to liquid N_2 temperature, the major phase of $MAPbBr_3$ NPLs retains its original cubic perovskite structure.

Atomic structure of the hybrid methylammonium bromide perovskite methylammonium lead bromide at freshly synthesized state

In general, the $MAPbBr_3$ NPLs structure observed in Figure 1 can be usually formed in a ~1h- to 9h-aging time at room temperature after synthesis to get an ideal single-crystalline. Owing to the fast

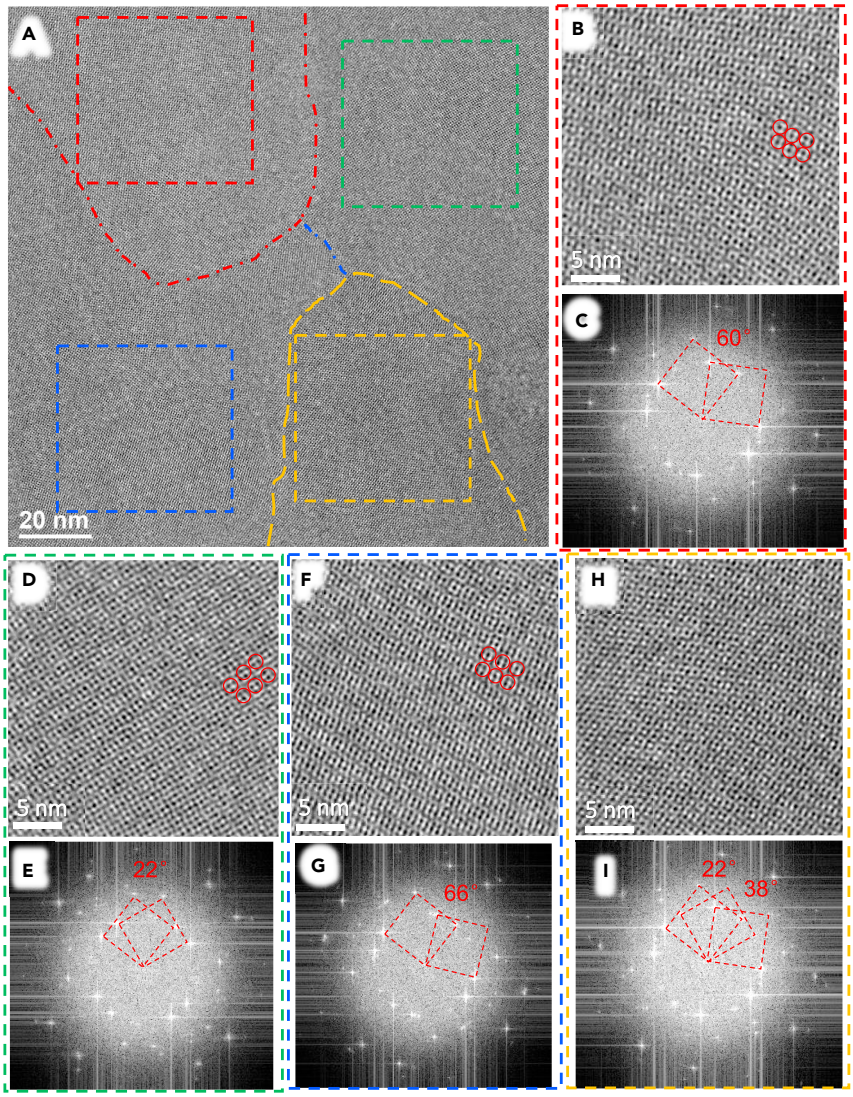

Figure 2. Investigations of the rotational Moiré fringes in fresh $MAPbBr_3$ NPLs

(A) Low electron dose cryo-HRTEM image (~6 e $Å^{-2}$ s^{-1}) of the fresh synthesized $MAPbBr_3$ NPLs along the [001] direction displaying four different rotational Moiré fringes overlapped by different $MAPbBr_3$ monolayers.

(B and C) Enlarged image of the selected area (red dashed box) in frame (A), illustrating the atomic structure of the 60° rotational Moiré fringes in the $MAPbBr_3$. Corresponding FFT patterns in C demonstrate that there are two sets of diffraction patterns for the [001] $MAPbBr_3$ monolayers with a 60° rotation angle.

(D–I) Enlarged image of the selected green (D), blue (F), and orange (H) dashed box areas in frame (A) show the other three type of rotational Moiré fringes patterns in the fresh synthesized $MAPbBr_3$ NPLs. Their corresponding FFT patterns (E, G, and I) depict the respective rotational angles: 22° for (D), 66° for (E), and 22° and 38° for (F).

formation process during the NPLs synthesis, two queries are arising in our mind: what the exact atomic structure of the $MAPbBr_3$ NPLs is at their freshly synthesized state (aging time <20 min), and whether they have already formed into the perfect single crystalline structure. Thus, we can further investigate the fine structure at the initial formation state of the MAPbBr3 NPLs in the cryo-TEM by the quickly cryogenic transfer method. Figure 2A shows an HRTEM image of the fresh synthesized $MAPbBr_3$ NPLs with typical Moiré fringes, although the differences in the Moiré fringes demonstrate that there are several overlapped $MAPbBr_3$ monolayers in the fresh synthesized NPLs (divided into four specific areas by the dashed lines). In the detail, four square boxes (red, green, blue, orange) have been selected to clearly show the Moiré fringes in Figures 2B and 2D–2F, respectively. For Figure 2B, the Moiré fringe patterns display long period lattices (outlined with red circles), which are

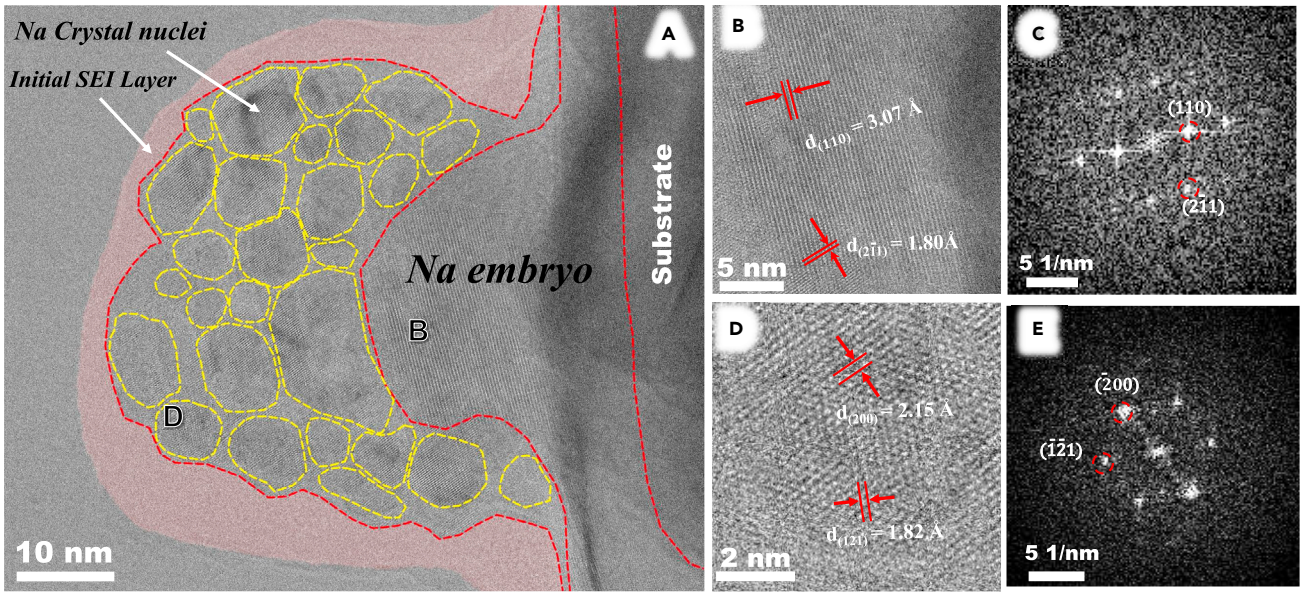

Figure 3. Investigations of Na dendrite nuclei with initial SEI layer in a Na metal battery

(A) Cryo-HRTEM image of a Na dendrite nuclei with initial SEI layer with an electron dose of ~11 e $Å^{-2}$ s^{-1}.

(B and C) Further enlarged HRTEM image of the Na embryo from (A) with the corresponding indexed FFT pattern given in (C).

(D and E) Enlarged HRTEM image of a Na nuclei particle from (A); the corresponding FFT pattern with indexes is shown in (E).

obviously different from the [001] $MAPbBr_3$ structure. The corresponding FFT pattern shown in Figure 2C demonstrates that there are two sets of [001] periodic patterns (outlined in red dashed squares) with a 60-degree rotation angle. Thus, the Moiré fringes shown in Figure 2B must have formed when two [001]-oriented $MAPbBr_3$ monolayers overlapped with a 60-degree rotation. Similarly, the enlarged HRTEM image in Figure 2D and corresponding FFT in Figure 2E show another type of Moiré fringe formed by the 22° rotation of two $MAPbBr_3$ monolayers, and Figures 2F and 2G show yet another Moiré fringe formed by the 66° rotation of two $MAPbBr_3$ monolayers. Interestingly, Figure 2H shows a rotational Moiré fringe comprised of three $MAPbBr_3$ monolayers at 22° and 38° rotation angles, determined by the corresponding FFT in Figure 2I. Furthermore, we also performed the selected area electron diffraction patterns of the freshly synthesized $MAPbBr_3$ NPLs shown in Figure S4, and it demonstrated the existence of the rotations in the [001] $MAPbBr_3$ structures. This result in well agreement with the observations in HRTEM and the corresponding FFT analyses. Therefore, we can conclude that fresh synthesized $MAPbBr_3$ NPLs consist of two or more single-crystalline monolayers along the [001] zone axis, which form the well-documented Moiré fringes. By the atomic characterization in cryo-TEM, we found an interesting structural evolution from an initial metastable state to the single crystalline of $MAPbBr_3$ NPLs during different material growth stages. The rotational Moiré fringes in the $MAPbBr_3$ NPLs may significantly impact its photoluminescence properties because the twisted lattice structure can significantly change the band structure in $MAPbBr_3$. Further investigations on this issue need to be carried out to understand the relationship between structural evolution and properties.

Na dendrite nuclei with initial solid electrolyte interphase layer structure in a sodium metal battery

Our second exemplar features alkali metals batteries (e.g., Li, Na, and K), whose solid-state electrolyte layers are highly sensitive to electron-beam characterization. Our cryo-HRTEM technique allowed us to capture images of the Na dendrite nuclei during its initial growth in the high-concentrated organic phosphate-based electrolyte. The diameter of the Na dendrite nuclei (yellow dashed areas) was about 4–10 nm, while the thickness of the outer SEI layer (labeled in pink) was approximately 6–10 nm (Figure 3A). The regions between the Na dendrite nuclei are disordered areas with amorphous matrix phase and dissociative weak lattices similar to Na crystal, which are considered as the semicrystalline areas before forming the Na dendrite nuclei. Surprisingly, the outer SEI layer consisted of an amorphous phase

only, which demonstrated that no inorganic crystalline components were formed in the early stage of the Na dendrite growth. The unmasked image of Figure 3A showing the initial SEI layer clearly is given in Figure S5. Furthermore, the X-ray photoelectron spectroscopy (XPS) spectra shown in Figure S7 reflect the chemical state of the deposited Na with its initial SEI layer through a vacuum transfer method from the glove box to the XPS system.

As shown in the right side of Figure 3A, a Na embryo with a lateral size of ~30 nm was formed in the center of the Na dendrite, surrounded by tiny Na crystal nuclei islands. The enlarged HRTEM and corresponding FFT images of the Na embryo (in Figures 3B–3C) are measured. The d-spacings are about 3.07 Å and 1.80 Å, which can be determined to be the planes of Na(110) and Na($2\bar{1}1$), respectively. The tiny Na crystal islands from Figure 3A were observed at atomic resolution in Figure 3D. The d-spacings were about 2.12 Å and 1.82 Å, which are belong to Na crystal planes of ($\bar{2}00$) and ($\bar{1}\bar{2}1$), respectively. The low electron dose cryo-TEM technique enables the structural investigations of the Na dendrite and its organic components which are easily broken under high-dose electron irradiation in conventional TEM. The native state of the initial SEI strongly suggests that organic solvent or electrolyte decomposition is pivotal to the early stage of SEI formation.

In conclusion, we performed atomic-scale characterization of organic–inorganic hybrid beam-sensitive materials using an ultra-low electron dose imaging method in the aberration corrected cryo-TEM. By stabilizing the sample at the temperature of liquid nitrogen and employing a low-dose detector, we achieve high-resolution characterization of the structures of organic–inorganic hybrid materials, which are often unstable in traditional HRTEM observations. We used cryo-TEM at the atomic scale to investigate both single-crystalline $MAPbBr_3$ NPLs and freshly prepared $MAPbBr_3$ with rotational Moiré fringes and observed an interesting structural evolution from an initial metastable state to the perfect crystalline of $MAPbBr_3$ NPLs. Our high-resolution cryo-TEM further enabled atomic-scale investigations of the native state of the initial Na nuclei-SEI and strongly suggested the participation of the solvent decomposition in the early stage of the SEI formation. This study facilitates investigations in a wide variety of beam-sensitive materials using cryo-TEM, offering important atomic structural information for organic–inorganic hybrid materials that will enable better design engineering.

Limitations of the study

There are several limitations when using the low-dose cryo-TEM method to investigate the microstructure of beam-sensitive materials. Like that in the conventional TEM, the sample thickness should be thin enough to perform the HRTEM experiments and the thinner samples make the better quality HRTEM images even in the low electron dose condition. As we can't use the double-tilt sample holder in the cryo-TEM, for the bulk material that needs to tuning the crystal axis to get HRTEM, it is hard to obtain good atomic structure images. It should be noted that cryo-TEM is operated at about 80 K, and phase transitions of some materials may occur during the cooling process at such low temperature, although such phase transformations are limited owing to the fast-cooling rates in our sample preparation. Cautions should be exercised for the phase identification based on cryo-TEM images. Therefore, this cryo-TEM technique used for characterizing electron beam-sensitive materials in the field of materials science is at its stage of development and needs to improve in the future.

STAR★METHODS

Detailed methods are provided in the online version of this paper and include the following:

- KEY RESOURCES TABLE
- RESOURCE AVAILABILITY
  - Lead contact
  - Materials availability
  - Data and code availability
- METHODS DETAILS
  - Preparation of $MAPbBr_3$ nanoplatelets
  - Preparation of Na battery
  - Cryo-transfer of TEM samples
  - Cryo-TEM characterization
  - Image processing and simulation

SUPPLEMENTAL INFORMATION

Supplemental information can be found online at https://doi.org/10.1016/j.isci.2021.103385.

ACKNOWLEDGMENTS

This work was supported by the Natural Science Foundation of China (Grant No. 12004156), and Shenzhen Basic Research Fund (JCYJ20190809181601639, 20200925154115001), Shenzhen Science and Technology Program (Grant No. KQTD20190929173815000), Guangdong Innovative and Entrepreneurial Research Team Program (Grant No. 2019ZT08C044). The TEM work used the resources of the Cryo-TEM Center, from SUSTech Core Research Facilities that receives support from the Shenzhen Municipality. Thanks for the samples provided by Dr. Shixun Wang, Prof. Andrey L. Rogach from City university of Hong Kong.

AUTHOR CONTRIBUTIONS

Y. Zhu and Q. Zhang contributed equally to this work. M. Gu and Y. Zhu designed the experiment. Y. Zhu performed the cryo-TEM experiments. Q. Zhang and M. Li prepared the Na cells for TEM. Y. Zhu and M. Gu conducted and analyzed the TEM data. Y. Zhu, Q. Zhang, B. Wang, and M. Gu wrote and revised the manuscript.

DECLARATION OF INTERESTS

The authors declare no competing interests.

Received: July 24, 2021
Revised: September 27, 2021
Accepted: October 26, 2021
Published: November 19, 2021

REFERENCES

Arenholz, E., Hsu, S.L., Yadav, A.K., Vishwanath, A., Schlepütz, C.M., Damodaran, A.R., Ramesh, R., Shafer, P., Clarkson, J.D., Dedon, L.R., et al. (2016). Observation of polar vortices in oxide superlattices. Nature *530*, 198–201. https://doi.org/10.1038/nature16463.

Bai, X., Yan, C., Yang, G., Lu, P., Ma, D., Sun, L., Zhou, R., Scheres, S.H.W., and Shi, Y. (2015). An atomic structure of human γ-secretase. Nature *525*, 212–217.

Chen, Q., Zhou, H., Fang, Y., Stieg, A.Z., Song, T.-B., Wang, H.-H., Xu, X., Liu, Y., Lu, S., You, J., et al. (2015). The optoelectronic role of chlorine in CH3NH3PbI3(Cl)-based perovskite solar cells. Nat. Commun. *6*, 7269. https://doi.org/10.1038/ncomms8269.

Chen, S., Zhang, X., Zhao, J., Zhang, Y., Kong, G., Li, Q., Li, N., Yu, Y., Xu, N., Zhang, J., et al. (2018). Atomic scale insights into structure instability and decomposition pathway of methylammonium lead iodide perovskite. Nat. Commun. *9*, 4807. https://doi.org/10.1038/s41467-018-07177-y.

Deng, Y.-H. (2021). Perovskite decomposition and missing crystal planes in HRTEM. Nature *594*, E6–E7. https://doi.org/10.1038/s41586-021-03423-4.

Egerton, R.F. (2012). Mechanisms of radiation damage in beam-sensitive specimens, for TEM accelerating voltages between 10 and 300 kV. Microsc. Res. Tech. *75*, 1550–1556.

Ghosh, S., Kumar, P., Conrad, S., Tsapatsis, M., and Mkhoyan, K.A. (2019). Electron-beam-damage in metal organic frameworks in the TEM. Microsc. Microanal. *25*, 1704–1705.

Han, B., Zhang, Z., Zou, Y., Xu, K., Xu, G., Wang, H., Meng, H., Deng, Y., Li, J., and Gu, M. (2021). Poor stability of Li2CO3 in the solid electrolyte interphase of a lithium-metal anode revealed by cryo-electron microscopy. Adv. Mater. *33*, 1–10. https://doi.org/10.1002/adma.202100404.

Hashimoto, A., Suenaga, K., Gloter, A., Urita, K., and Iijima, S. (2004). Direct evidence for atomic defects in graphene layers. Nature *430*, 870–873.

Hayat, M.A.E. (2012). Basic Techniques for Transmission Electron Microscopy (Elsevier).

Hong, H., Zhang, J., Zhang, J., Qiao, R., Yao, F., Cheng, Y., Wu, C., Lin, L., Jia, K., Zhao, Y., et al. (2018). Ultrafast broadband charge collection from clean graphene/CH3NH3PbI3 interface. J. Am. Chem. Soc. *140*, 14952–14957. https://doi.org/10.1021/jacs.8b09353.

Lei, Y., Chen, Y., Zhang, R., Li, Y., Yan, Q., Lee, S., Yu, Y., Tsai, H., Choi, W., Wang, K., et al. (2020). A fabrication process for flexible single-crystal perovskite devices. Nature *583*, 790–795. https://doi.org/10.1038/s41586-020-2526-z.

Li, Y., Huang, W., Li, Y., Pei, A., Boyle, D.T., and Cui, Y. (2018). Correlating structure and function of battery interphases at atomic resolution using cryoelectron microscopy. Joule *2*, 2167–2177. https://doi.org/10.1016/j.joule.2018.08.004.

Lin, Z.-J., Lü, J., Hong, M., and Cao, R. (2014). Metal–organic frameworks based on flexible ligands (FL-MOFs): Structures and applications. Chem. Soc. Rev. *43*, 5867–5895.

Ran, J., Dyck, O., Wang, X., Yang, B., Geohegan, D.B., and Xiao, K. (2020). Electron-beam-related studies of halide perovskites: Challenges and opportunities. Adv. Energy Mater. *10*, 1903191.

Rothmann, M.U., Kim, J.S., Borchert, J., Lohmann, K.B., O'Leary, C.M., Sheader, A.A., Clark, L., Snaith, H.J., Johnston, M.B., Nellist, P.D., and Herz, L.M. (2020). Atomic-scale microstructure of metal halide perovskite. Science *370*, eabb5940. https://doi.org/10.1126/science.abb5940.

Rothmann, M.U., Li, W., Zhu, Y., Liu, A., Ku, Z., Bach, U., Etheridge, J., and Cheng, Y.B. (2018). Structural and chemical changes to CH3NH3PbI3 induced by electron and gallium ion beams. Adv. Mater. *30*, 1800629. https://doi.org/10.1002/adma.201800629.

Sawada, H., Sasaki, T., Hosokawa, F., and Suenaga, K. (2015). Atomic-resolution STEM imaging of graphene at low voltage of 30 kV with resolution enhancement by using large convergence angle. Phys. Rev. Lett. *114*, 166102.

Stock, N., and Biswas, S. (2012). Synthesis of metal-organic frameworks (MOFs): Routes to various MOF topologies, morphologies, and composites. Chem. Rev. *112*, 933–969.

Wang, X., Li, Y., and Meng, Y.S. (2018). Cryogenic electron microscopy for characterizing and diagnosing batteries. Joule *2*, 2225–2234. https://doi.org/10.1016/j.joule.2018.10.005.

Weidman, M.C., Goodman, A.J., and Tisdale, W.A. (2017). Colloidal halide perovskite nanoplatelets: An exciting new class of semiconductor nanomaterials. Chem. Mater. *29*, 5019–5030. https://doi.org/10.1021/acs.chemmater.7b01384.

Williams, D.B., and Carter, C.B. (1996). Transmission Electron Microscopy (Springer).

Yang, S., Niu, W., Wang, A.-L., Fan, Z., Chen, B., Tan, C., Lu, Q., and Zhang, H. (2017). Ultrathin two-dimensional organic-inorganic hybrid perovskite nanosheets with bright, tunable photoluminescence and high stability. Angew. Chem. Int. Ed. *56*, 4252–4255. https://doi.org/10.1002/anie.201701134.

Ye, M., Hu, S., Zhu, Y., Zhang, Y., Ke, S., Xie, L., Zhang, Y., Hu, S., Zhang, D., Luo, Z., et al. (2021). Electric polarization switching on an atomically thin metallic oxide. Nano Lett. *21*, 144–150. https://doi.org/10.1021/acs.nanolett.0c03417.

Zhu, Y., Gui, Z., Wang, Q., Meng, F., Feng, S., Han, B., Wang, P., Huang, L., Wang, H.L., and Gu, M. (2020a). Direct atomic scale characterization of the surface structure and planar defects in the organic-inorganic hybrid CH3NH3PbI3 by Cryo-TEM. Nano Energy *73*, 104820. https://doi.org/10.1016/j.nanoen.2020.104820.

Zhu, Y., Liu, L., Cao, G., Xing, W., Chu, Y.H., Zhu, J., and Yu, R. (2020b). Atomic structure and properties of a perovskite/spinel (111) interface. Phys. Rev. B *102*, 165302. https://doi.org/10.1103/PhysRevB.102.165302.

STAR★METHODS

KEY RESOURCES TABLE

REAGENT or RESOURCE	SOURCE	IDENTIFIER
Chemicals, peptides, and recombinant proteins		
$PbBr_2$	Macklin	http://www.macklin.cn/products/L837027
MAI	Aladdin	https://www.aladdin-e.com/zh_cn/m157987.html
n-octylamine	Aladdin	https://www.aladdin-e.com/zh_cn/o110546.html
DMF	Aladdin	https://www.aladdin-e.com/zh_cn/d301788.html
Toluene	Sigma-Aldrich	https://www.sigmaaldrich.cn/CN/zh/product/sigald/179418?context=product
NaFSI	Aladdin	https://www.aladdin-e.com/zh_cn/s161088.html
trimethyl phosphate	Macklin	http://www.macklin.cn/products/T818846
Na metal	Aladdin	https://www.aladdin-e.com/zh_cn/s108763.html
copper grid	TED PELLA	https://www.tedpella.com/grids_html/gilder.htm#anchor1540234
Software and algorithms		
MacTempas X	Total Resolution LLC	https://www.totalresolution.com/
DigiitalMicrograph	Gatan Inc	https://www.gatan.com/
Other		
XPS	ULVAC-PHI	https://www.ulvac-phi.com/en/products/xps/versaprobe-iii/
Cryo TEM	Thermofisher Inc	https://www.thermofisher.cn/cn/zh/home.html

RESOURCE AVAILABILITY

Lead contact

Further information and requests for resources and reagents should be directed to and will be fulfilled by the lead contact, M. Gu (gum@sustech.edu.cn).

Materials availability

This study did not generate new unique reagents.

Data and code availability

Microscopy data reported in this paper will be shared by the lead contact upon request and they are publicly available as of the date of publication.

This paper does not report original code.

Any additional information required to reanalyze the data reported in this paper is available from the lead contact upon request.

METHODS DETAILS

Preparation of $MAPbBr_3$ nanoplatelets

0.4 mmol $PbBr_2$, 0.4 mmol MAI, and 0.7 mmol n-octylamine were added into 800 μl DMF solution in a 3 ml glass vial in a glove box, under vigorous shaking. 5 μl of the above precursor was swiftly added at room temperature into 1 ml of toluene to form the fresh $MAPbBr_3$ NPLs, which were subjected to aging for 1-9 h at room temperature to achieve aged samples. For the fresh synthesized samples in Figure 2, the aging time is less than 20 minutes, containing the preparation time of TEM sample.

Preparation of Na battery

The electrolyte for this experiment was NaFSI (Macklin, 99.9%) in trimethyl phosphate (Macklin, 98%) with the salt-to-solvent molar ratio of 1:2.69. The type-2032 coin-cells were assembled with Na metal (ΦNa electrode = 12mm, TED PELLA, INC., 99.99%) as the counter electrode and copper foil (Φcopper foil = 12mm, Kermel, 99.99%) as working electrode. The copper grid (TED PELLA, INC.) was placed on the copper foil side for collecting the Na dendrites. The Na | Cu coin-cells were charged for 1h at the current density of 1.0 mA cm^{-2}. The specimen for XPS experiment was transferred directly from the glove box to the XPS chamber via a vacuum transfer method for reliable data collection.

Cryo-transfer of TEM samples

We applied cryo-TEM sample preparation and cryotransfer steps as outlined in Figure S1. Samples were dropped on a lacey carbon film supported TEM-grid inside the Ar-filled glove box, dried for a while and the specimen was immediately immersed into a liquid nitrogen box in the glove box. Thus, the specimen was protected and sealed by the liquid nitrogen before it was taken out. Then, the specimen in the liquid nitrogen box was taken out and transferred into a cryo-transfer auto-loader. At last, the TEM specimen was inserted into the cryogenic chamber of the cryo-TEM through the cryo-transfer auto-loader. This was done to ensure that the sensitive materials were completely isolated from any trace of oxygen/ moisture from the environment.

Cryo-TEM characterization

Cryo-TEM images were acquired on a Titan Krios G3i 5 cryo-TEM operated at 300kV and equipped with an objective Cs corrector, using a direct electron detect camera (Falcon 2, Thermo Fisher Scientific Ltd.). The dose rate for each cryo-TEM image was kept below 0.3 e $Å^{-2}$ s^{-1} for the low magnification images and ~ 2-4 e $Å^{-2}$ s^{-1} for high-resolution images, respectively. To decrease the dose rate, 32 continuous frames were acquired within 2-5 seconds and then integrated into one image by a drift-correction plug-in script.

Image processing and simulation

To improve the signal-to-noise ratio of the HRTEM images, Weiner Filter and Average Background Subtraction Filter were used to denoise the images. Simulation of TEM images was carried out using commercial software (MacTempas) based on a multislice algorithm. The adopted crystal structure of $MAPbBr_3$ was the cubic phase with the lattice parameters $a=b=c$=5.9195 Å. Simulation parameters were set according to the experimental TEM conditions (convergence angle= 0.05 mrad, spherical aberration C_3=-0.006 mm, accelerating voltage= 300 kV).